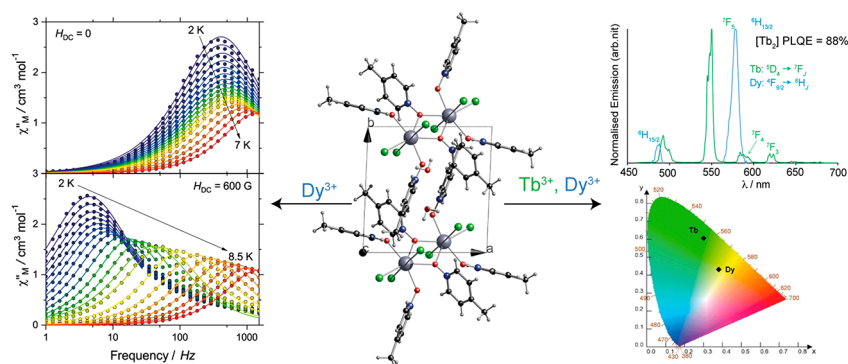


# Binuclear Lanthanide Complexes Based on 4-Picoline-*N*-oxide: From Sensitized Luminescence to Single-Molecule Magnet Characteristics

Senthil Kumar Kuppusamy,\* Eufemio Moreno-Pineda,\* Aline M. Nonat,\* Benoît Heinrich, Lydia Karmazin, Loïc J. Charbonnière, and Mario Ruben\*



**ABSTRACT:** Lanthanide complexes featuring luminescent and/or single-molecule magnet (SMM) characteristic(s) are proposed candidates to develop molecule-based spintronics, memory, and quantum information processing (QIP) device architectures. Herein, we report on the luminescent and/or SMM characteristic(s) of charge-neutral binuclear lanthanide complexes— $[\text{Ln}_2\text{Cl}_6(4\text{-picNO})_4(\mu_2\text{-}4\text{-picNO})_2] \cdot 2\text{H}_2\text{O}$  ( $\text{Ln}^{3+} = \text{Tb}^{3+}$  ([Tb<sub>2</sub>]) or  $\text{Dy}^{3+}$  ([Dy<sub>2</sub>]); 4-picNO = 4-picoline-*N*-oxide). The Dy and Tb complexes show 4-picNO-sensitized luminescence with quantum yields in the solid state of 0.14% and 88%, respectively. The luminescent Dy complex is an SMM with a magnetization reversal barrier ( $U_{\text{eff}} = 20.6(4) \text{ cm}^{-1}$ ) under zero applied magnetic field, whereas the Tb complex is not an SMM. The facile preparation of  $[\text{Ln}_2\text{Cl}_6(4\text{-picNO})_4(\mu_2\text{-}4\text{-picNO})_2] \cdot 2\text{H}_2\text{O}$  complexes showing high luminescence quantum yield (Tb<sup>3+</sup>) and SMM characteristics (Dy<sup>3+</sup>) might prove useful toward the designing of analogue luminescent-SMM hybrids suitable for technological applications.

## INTRODUCTION

Lanthanide ( $\text{Ln}^{3+}$ ) complexes exhibiting single-molecule magnet (SMM)<sup>1–3</sup> and/or line-like emission behavior<sup>4,5</sup> are plausible molecular systems for the fabrication of miniaturized information storage,<sup>1,6–8</sup> computing,<sup>9–12</sup> and spintronics<sup>13–17</sup> device architectures via bottom-up self-assembly approaches. Consequently, continuous efforts to modulate the SMM<sup>18–23</sup> and luminescent properties<sup>24,25</sup> of  $\text{Ln}^{3+}$  complexes by ligand field tuning and molecular energy level engineering, respectively, are in progress to harness the application potential of the  $\text{Ln}^{3+}$  complexes.<sup>26,27</sup>

Lanthanide-SMMs (Ln-SMMs), especially Dy<sup>3+</sup>-based SMMs,<sup>28–37</sup> possessing large intrinsic magnetic anisotropy and slow relaxation of the magnetization, have been proposed to perform as quantum bits (qubits)—the quantum unit of information.<sup>10,12,38–40</sup> While the classical binary digits (bits) are limited to values of 0 or 1, qubits can additionally take-up

superposition of 0 or 1; that is, the state of a single qubit is a linear combination of 0 and 1, offering enhanced information processing ability compared to classical bits. Coupling of individual qubits into arrays is a strategy adopted to fabricate quantum gates for quantum computing applications.<sup>41–43</sup> However, difficulties inherent to the interqubit coupling limits the utility of such a strategy. As an alternative, for example, the exponential extension of Hilbert space<sup>41</sup> can be achieved employing the nuclear states of the lanthanides by designing bi- or multinuclear isotopologues Ln-SMMs.<sup>9,10,41</sup> The hyper-

fine coupling between the nuclear spin and the ground doublet in Ln-SMMs composed of isotopically enriched Ln<sup>3+</sup> centers, for example, <sup>163</sup>Dy ( $I = 5/2$ ) or the indirect coupling of nuclear states<sup>10,44</sup> produces different quantum states (extension of Hilbert space), enabling the construction of multilevel systems termed as qudits, where  $d > 2$ .<sup>44–46</sup> The hyperfine split qudit levels are addressed taking advantage of the quantum tunnelling of magnetization (QTM), as exemplified in the case of prototypical Tb-complexes.<sup>10,16,44,47</sup> It is evident that a binuclear SMM could function as a multilevel qudit system in the presence of QTM and hyperfine interactions, and such a system is desirable for quantum information processing (QIP) applications.<sup>10,44</sup>

In addition to the SMM property, Ln<sup>3+</sup>-based, for example, Ln<sup>3+</sup> = Eu, Tb, Dy, Er, or Yb, mono-, bi-, and multinuclear complexes feature intense, long-lived, and line-like sensitized emission bands covering the whole visible and IR spectral range.<sup>4,5,24,48–53</sup> The alluring emission characteristics render luminescent Ln<sup>3+</sup> complexes suitable for developing multifunctional<sup>26,27</sup> molecule-based optical data-storage and communication systems.<sup>54–57</sup> Crucially, the emission properties coupled with the presence of nuclear spins enables the creation of Ln<sup>3+</sup>-molecule-based coherent light-matter interfaces. Such interfaces can be leveraged to demonstrate the quantum information processing utility of the luminescent lanthanide complexes. Recently, we have reported on the creation of coherent light-matter interfaces in binuclear and mononuclear Eu<sup>3+</sup> complexes.<sup>58,59</sup> We have shown that spectral holes can be burnt in the electric dipole-induced <sup>5</sup>D<sub>0</sub>-to-<sup>7</sup>F<sub>0</sub> transition, enabling the estimation of the optical coherence lifetime ( $T_2$ ) and polarization of nuclear spins in one of the ground-state hyperfine levels.<sup>58</sup> Moreover, by taking advantage of the ultranarrow <sup>5</sup>D<sub>0</sub>-to-<sup>7</sup>F<sub>0</sub> inhomogeneous line width associated with a mononuclear Eu<sup>3+</sup> complex, we have demonstrated storage of photons inside a molecular crystal, rendering the complex as an optically addressable molecular memory. Crucially, the utility of the Eu<sup>3+</sup> complex as a scalable qubit architecture—useful for performing quantum gate operations—has been elucidated by quantifying controlled ion–ion interactions between the Eu<sup>3+</sup> centers.<sup>59</sup> All the prototypical demonstrations listed above elucidate the QIP utility of the Ln<sup>3+</sup>-based molecular systems.

It is evident from the above discussions that Ln<sup>3+</sup> complexes featuring SMM and/or luminescent characteristics are useful systems for developing application-oriented materials.<sup>60,61</sup> Ln<sup>3+</sup> systems featuring both SMM and luminescent properties are ideal model systems to probe magneto-luminescence correlations, which may lead to light addressable SMMs both in the bulk and on the surface.<sup>62–65</sup> By analyzing the fine structure associated with the luminescent line corresponding to the ground state term, for example,  $m_J = 15/2$  in Dy<sup>3+</sup>, induced by ligand field (Stark splitting), the energy separation between the ground and excited  $m_J$  levels can be inferred as has been demonstrated.<sup>66,67</sup> On the other hand, the narrow spectral line widths associated with Ln<sup>3+</sup> systems could be leveraged to develop QIP systems.

In this context, we have extended on our previous report concerning [Eu<sub>2</sub>Cl<sub>6</sub>(4-picNO)<sub>4</sub>(μ<sub>2</sub>-4-picNO)<sub>2</sub>].2H<sub>2</sub>O and prepared two new binuclear complexes—[Ln<sub>2</sub>Cl<sub>6</sub>(4-picNO)<sub>4</sub>(μ<sub>2</sub>-4-picNO)<sub>2</sub>].2H<sub>2</sub>O; Ln = Tb<sup>3+</sup> [Tb<sub>2</sub>] or Dy<sup>3+</sup> [Dy<sub>2</sub>] and studied their magnetic and luminescent characteristics, as detailed in the following sections.

## RESULTS AND DISCUSSION

**Synthesis and Crystal Structures.** The binuclear Ln<sup>3+</sup> complexes discussed in this study are prepared by following a procedure reported for [Ln<sub>2</sub>Cl<sub>6</sub>(4-picNO)<sub>4</sub>(μ<sub>2</sub>-4-picNO)<sub>2</sub>].2H<sub>2</sub>O (Ln = Eu<sup>3+</sup> or Gd<sup>3+</sup>).<sup>58</sup> See [Experimental Section](#) and [Supporting Information](#) (Figure S1 and Table S1) for more details.

X-ray crystallographic analyses revealed that the complexes crystallize in the centrosymmetric  $P\bar{1}$  space group belonging to the triclinic crystal system (Table S2). As a representative example, the crystal structure of [Dy<sub>2</sub>Cl<sub>6</sub>(4-picNO)<sub>4</sub>(μ<sub>2</sub>-4-picNO)<sub>2</sub>].2H<sub>2</sub>O is detailed (Figure 1), and the crystal

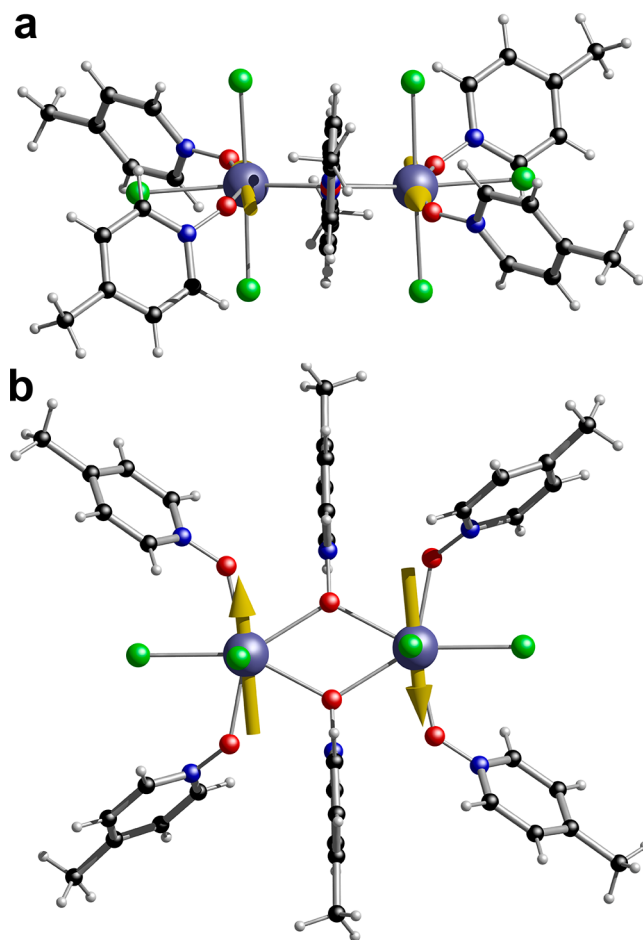


**Figure 1.** X-ray crystal structure of [Dy<sub>2</sub>Cl<sub>6</sub>(4-picNO)<sub>4</sub>(μ<sub>2</sub>-4-picNO)<sub>2</sub>].2H<sub>2</sub>O. (a) Side view and (b) top view. The arrows show the direction of the principal axis of the  $g$ -tensor in the ground Kramer doublet of the Dy-complex, obtained from CASSCF calculations. Color code: Dy, blue; C, black; Cl, green; O, red; H, light gray.

structure and related parameters of [Tb<sub>2</sub>Cl<sub>6</sub>(4-picNO)<sub>4</sub>(μ<sub>2</sub>-4-picNO)<sub>2</sub>].2H<sub>2</sub>O is depicted in the [Supporting Information](#) (Figure S2 and Table S2). The neutral [Dy<sub>2</sub>] is composed of six 4-picNO and six chloride ligands. The O<sub>4</sub>Cl<sub>3</sub> coordination environment around each Dy<sup>3+</sup> ion is best described as pentagonal bipyramidal with a continuous shape measure (CShM) of 1.513. The equatorial positions (edges) of each pentagonal bipyramid are occupied by two monodentate 4-picNO ligands in *trans* fashion, one chloride ligand, and two μ<sub>2</sub>-4-picNO ligands. The axial positions of each pentagonal bipyramid are occupied by the remaining chloride ligands. The

Dy–O bond lengths range from 2.264(3) Å to 2.461(2) Å. The Dy–O bond lengths involving monodentate 4-picNO ligands are shorter than the Dy–O bond lengths associated with the  $\mu_2$ -4-picNO ligands. The Dy–Cl bond lengths, with values ranging from 2.6598(10) Å to 2.7000(9) Å, are longer than the Dy–O bond lengths. The Dy–Cl bond lengths—2.6598(10) Å and 2.6714(10) Å—of the axial chloride ligands are shorter than the equatorial Dy–Cl bond length—2.7000(9) Å. The intramolecular Dy–Dy and the shortest intermolecular Dy–Dy distances are 4.2237(4) Å and 8.3813(6) Å, respectively.

The Tb complex showed similar Ln–O, Ln–O( $\mu_2$ ) and Ln–Cl bond lengths as observed for [Dy<sub>2</sub>]. Intramolecular Tb–Tb and shortest intermolecular Tb–Tb distances of 4.2270(4) Å and 8.3727(5) Å, respectively, are observed.

In the crystal lattice, the complex molecules—[Dy<sub>2</sub>] or [Tb<sub>2</sub>]—arrange into layers in the  $b \times c$  plane with two cocrystallized water molecules (Figure 2), according to an

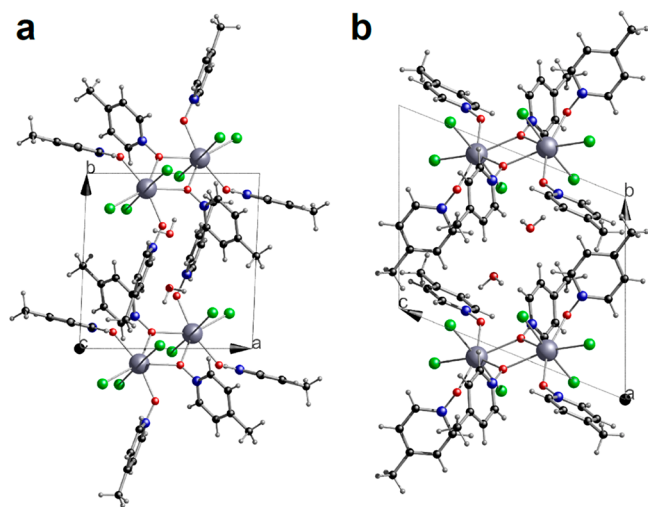


**Figure 2.** Arrangement of [Dy<sub>2</sub>] in the crystalline state at 173 K (a) along the crystallographic  $c$ -axis and (b) along  $a$ -axis, as obtained from the single-crystal XRD data. The arrangement of [Tb<sub>2</sub>] is not shown because the complex organizes in the same way in the crystalline state as [Dy<sub>2</sub>].

oblique  $P\bar{1}$  lattice (one molecule per asymmetric unit). Successive layers superpose with constant lateral shift leading to single-layer periodicity and a triclinic structure with one molecule per unit cell.

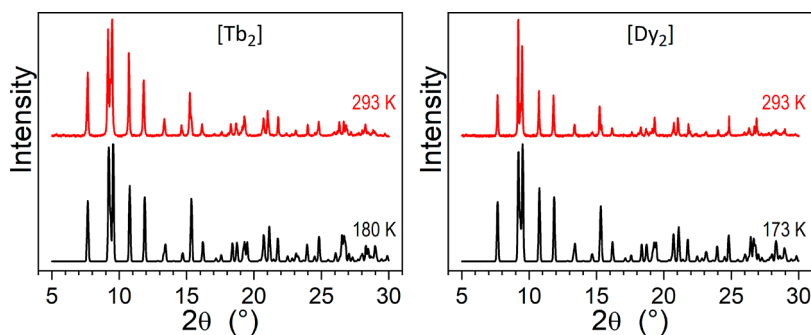


**Figure 3.** Experimental PXR D patterns of [Tb<sub>2</sub>] (left) and [Dy<sub>2</sub>] (right) at room temperature (top, red), as compared to the patterns calculated from the single-crystal X-ray structures of the complexes (bottom, black). All patterns are composed of the same reflections with only small changes in peak position and intensity, in relation with small variations of lattice parameters and electron densities.

**Powder X-ray Diffraction (PXR D) Studies.** To study the phase purity of the crystalline complexes, PXR D measurements of the complexes were performed. A good match observed between the PXR D and single-crystal (SCXR D) patterns (Figure 3) of the complexes elucidates the phase purity of the crystalline complexes. Comparable unit cell parameters (Figure S3 and Table S3) obtained from the indexing of the PXR D and SCXR D data serve as an additional proof confirming the phase purity of the complexes.

In the powder, the molecular volume regularly decreases, at a mean rate of 4.3 Å<sup>3</sup> per atomic number, from Eu-to-Dy (Table S3), which involves a decrease of layer spacing ( $\Delta d/d$  jumps of 0.13–0.14%) and of lateral distances ( $\Delta(\sqrt{A})/\sqrt{A}$ ) changes of 0.11–0.12%). Single-crystal structures follow analogous trends (Table S3), although parameter values are more dispersed. The cell volume, sublattice area, and layer spacing vary with the nature of the Ln<sup>3+</sup> ion, within respectively 1.5%, 1.2%, and 0.5% in the powder structures. At the same time, the  $\sqrt{A}/d$  ratio is nearly constant ( $1.179 \pm 0.001$ ), as well as parameter  $a$  of in-plane arrangement ( $66.61 \pm 0.04^\circ$ ) and the shift of successive molecular layers related to  $b$  and  $c$  ( $3.20 \pm 0.03$  Å). This confirms the equivalence of all structures, with only small changes of lattice parameters.

**Photophysical Studies.** The photoluminescence characteristics of the complexes were studied in the solid state by exciting the 4-picNO-based transition centered at  $\sim 330$  nm. At room temperature, [Tb<sub>2</sub>] showed a bright luminescence corresponding to the  $^5D_4 \rightarrow ^7F_J$  ( $J = 6-3$ ) transitions with weaker emission bands in the 640–660 nm region corresponding to  $J = 2$  to 0 (Figure 4a). A high quantum yield of 88% (Table 1) evidences a very good sensitization of the  $^5D_4$  level of Tb<sup>3+</sup> by 4-picNO. The PL of the terbium complex decays monoexponentially with a lifetime of 1.32 ms (Figure S4), indicating the presence of a single emissive species. The Dy complex showed weak Dy<sup>3+</sup> centered emission bands at 485 nm ( $^4F_{9/2} \rightarrow ^6H_{15/2}$ ), 577 nm ( $^4F_{9/2} \rightarrow ^6H_{13/2}$ ), 663 nm ( $^4F_{9/2} \rightarrow ^6H_{11/2}$ ), 754 nm ( $^4F_{9/2} \rightarrow ^6H_{9/2}$ ), and 833 nm ( $^4F_{9/2} \rightarrow ^6H_{7/2}$ ) as shown in Figures 4a and S5a. A quantum yield of  $\sim 0.14\%$  and lifetime ( $\tau$ )  $< 10$   $\mu$ s were observed upon ligand excitation at 339 nm at room temperature; accurate determination of the lifetime was prevented by low signal intensity. At 77 K, a lifetime of 4.8  $\mu$ s could be determined (Figure S5b). A low-symmetry crystal field around Dy<sup>3+</sup> in [Dy<sub>2</sub>] is inferred from the PL spectrum shown in Figure 4. The intensity of the blue  $^4F_{9/2} \rightarrow ^6H_{15/2}$  magnetic dipole transition centered at 485 nm hardly varies

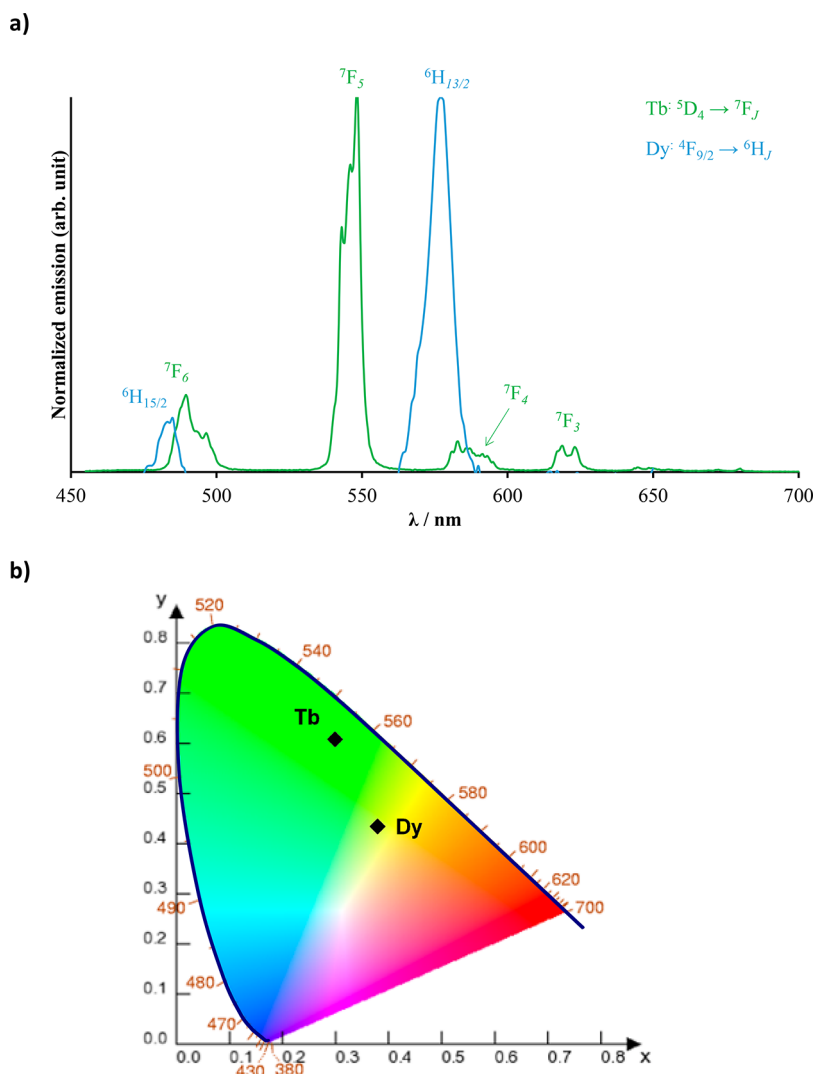


**Figure 4.** Steady-state emission characteristics of [Tb<sub>2</sub>] and [Dy<sub>2</sub>]. (a) Normalized RT emission spectra of [Tb<sub>2</sub>] ( $\lambda_{\text{exc}} = 330$  nm) and [Dy<sub>2</sub>] ( $\lambda_{\text{exc}} = 339$  nm) complexes in the solid state and (b) the Commission Internationale de l'éclairage (CIE) color space chromaticity diagram of the complexes in the solid state (Tb:  $x = 0.3032$ ,  $y = 0.6092$ ; Dy:  $x = 0.3835$ ,  $y = 0.4325$ ).

**Table 1. Selected Photophysical Data of [Tb<sub>2</sub>] and [Dy<sub>2</sub>] Complexes in the Solid State**

complex	$\Delta E$ (cm <sup>-1</sup> )	$\tau_{\text{obs}}$ (μs) <sup>a</sup>	$\phi_{\text{tot}}$ (%) <sup>b</sup>
[Tb <sub>2</sub> ]	3310	1330	88
[Dy <sub>2</sub> ]	2980	<10	0.14

<sup>a</sup> $\lambda_{\text{exc}} = 330$  nm for [Tb<sub>2</sub>] and 339 nm for [Dy<sub>2</sub>]. <sup>b</sup>Error for the absolute determination of quantum yield is estimated to be  $\pm 15\%$ .

with the crystal field around Dy<sup>3+</sup> ions, whereas the electric dipolar transition (<sup>4</sup>F<sub>9/2</sub> → <sup>6</sup>H<sub>13/2</sub>) at 577 nm is hypersensitive to the Dy<sup>3+</sup> coordination environment and is dominant for low local-site symmetry species, according to the Judd–Ofelt theory.<sup>68</sup> The observation of weak emission around 665 nm (<sup>4</sup>F<sub>9/2</sub> → <sup>6</sup>H<sub>11/2</sub>) also evidences the low symmetry of the crystal field around Dy<sup>3+</sup> in [Dy<sub>2</sub>].

The observed trends in the luminescence sensitization emission from [Tb<sub>2</sub>] and [Dy<sub>2</sub>] can be rationalized considering the triplet energy ( $E_T$ ) of the 4-picNO antenna. An  $E_T = 23810$  cm<sup>-1</sup> (420 nm) was estimated (Figure S6), as reported in our previous study.<sup>48</sup> The triplet level of 4-picNO is located above the receiving levels of Tb<sup>3+</sup> (<sup>5</sup>D<sub>4</sub> = 20500 cm<sup>-1</sup>) and Dy<sup>3+</sup>

(<sup>4</sup>F<sub>9/2</sub> = 20830 cm<sup>-1</sup>). This implies that the energy transfer from the triplet level of 4-picNO to the <sup>5</sup>D<sub>4</sub> and <sup>4</sup>F<sub>9/2</sub>, receiving levels of Tb<sup>3+</sup> and Dy<sup>3+</sup>, respectively, led to the sensitized luminescence. The total ligand to metal sensitization energy transfer efficiency ( $\eta_{\text{sens}}$ ) depends on the energy gap ( $\Delta E$ ) between the triplet state of the donor and Ln<sup>3+</sup> acceptor states. An energy gap of  $2500$  cm<sup>-1</sup> <  $\Delta E(^3\pi\pi - ^5D_4)$  <  $4000$  cm<sup>-1</sup> is reported ideal for the luminescence sensitization of Tb<sup>3+</sup>. The high PL quantum yield of 88% observed for [Tb<sub>2</sub>] is likely facilitated due to an optimal energy separation— $\Delta E \approx 3310$  cm<sup>-1</sup>—between the triplet level of 4-picNO and the <sup>5</sup>D<sub>4</sub> acceptor level of Tb<sup>3+</sup>. On the other hand, an optimal  $\Delta E$  is not established for Dy<sup>3+</sup> complexes. The presence of thermally accessible levels lying above the receiving <sup>4</sup>F<sub>9/2</sub> level and the possible thermal back-energy transfer between the <sup>4</sup>F<sub>9/2</sub> level and energetically close-lying excited levels is attributed as a contributing factor, decreasing the sensitized luminescence quantum yield of Dy-complexes.<sup>63</sup>

**Magnetic Properties of the Complexes.** Direct current (DC) magnetic susceptibility studies of [Gd<sub>2</sub>],<sup>58</sup> [Tb<sub>2</sub>], and [Dy<sub>2</sub>] complexes were carried out in an applied field ( $H_{\text{dc}} = 0.1$  T. At 300 K,  $\chi_M T$  values of 15.8 ([Gd<sub>2</sub>]), 28.1 ([Dy<sub>2</sub>]), and

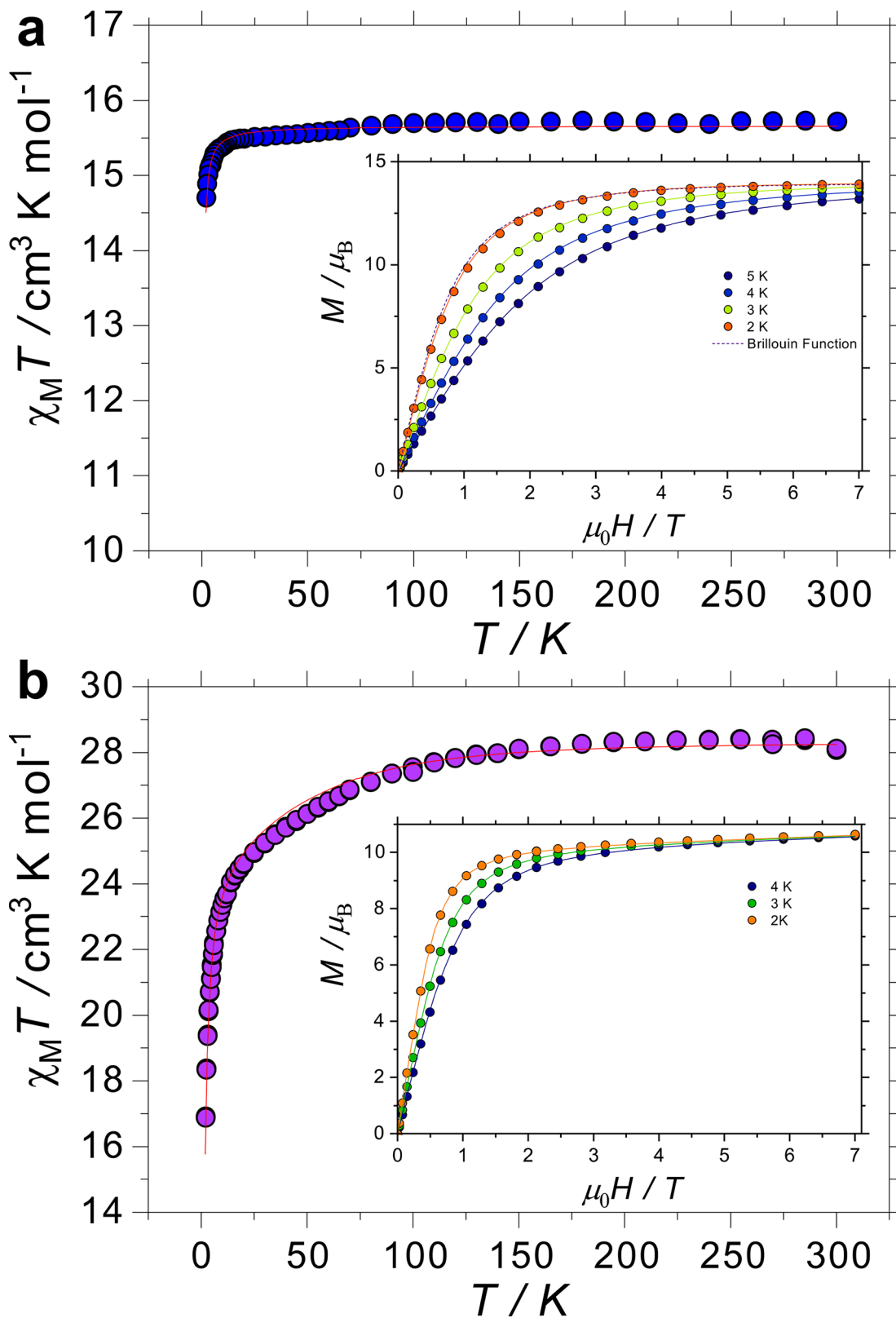


**Figure 5.** (a) Experimental  $\chi_M T(T)$  plot of  $[\text{Gd}_2]$  at an applied DC field of 0.1 T and magnetization ( $M(H)$ ) (inset) (solid symbols) and simulations (solid lines) obtained after simultaneous fitting employing eq 1; (b) experimental  $\chi_M T(T)$  plots of  $[\text{Dy}_2]$  at  $H_{\text{DC}} = 0.1 \text{ T}$  and magnetization ( $M(H)$ ) (inset) (solid symbols) and simulations (solid lines) obtained by simultaneous fitting employing eq 3, CF parameters obtained from CASSCF calculation, and an isotropic interaction connecting the spin part of the Dy(III) ions.

23.4 ( $[\text{Tb}_2]$ )  $\text{cm}^3 \text{K mol}^{-1}$  are observed (Figures 5 and S7). The  $\chi_M T$  values are in the range expected for two uncoupled lanthanide ions. For  $[\text{Gd}_2]$ , the  $\chi_M T$  versus  $T$  plot stays

practically constant upon cooling down to  $\sim 10 \text{ K}$ . Further cooling resulted in a decrease of the  $\chi_M T$  product. A gradual decrease of the  $\chi_M T$  product is observed for the  $[\text{Tb}_2]$  and

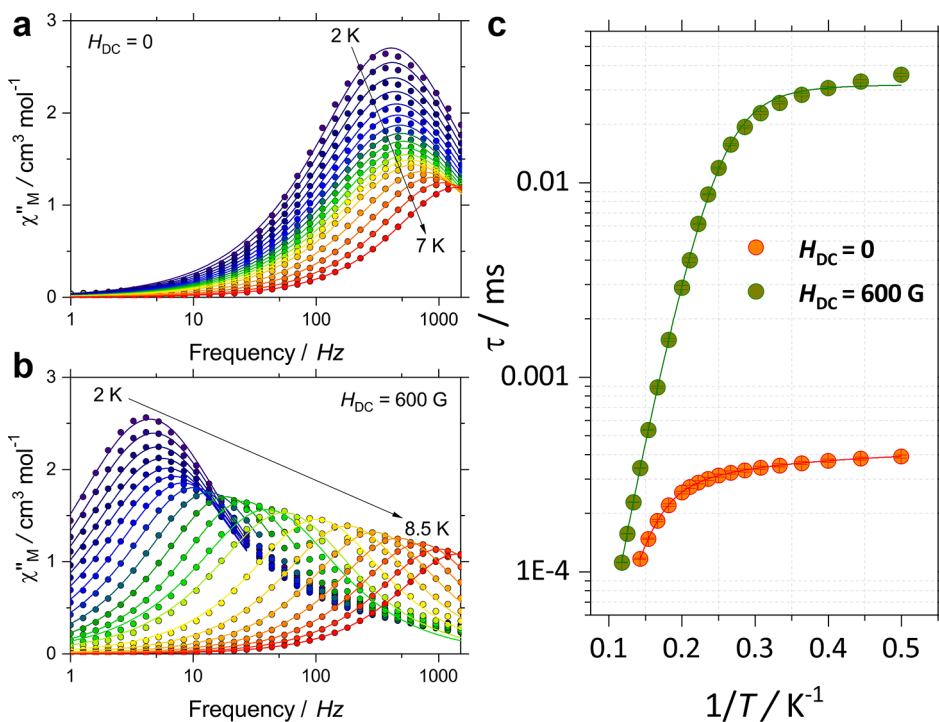


**Figure 6.** Single-molecule magnet characteristics of  $[\text{Dy}_2]$ . (a)  $\chi_M''(\nu)$  at zero applied magnetic field and; (b)  $\chi_M''(\nu)$  for  $H_{\text{DC}} = 600$  Oe; (c) temperature dependence of the relaxation times  $\tau(T)$  (symbols) and the fitting using eq 2 and parameters in the text. The corresponding  $\chi_M''(\nu)$  and Cole–Cole plots are shown in Figures S0 and S11.

$[\text{Dy}_2]$  complexes down to 100 K. Cooling the samples further causes a faster decrease of the  $\chi_M T$  products, indicating the depopulation of the crystal field levels and/or antiferromagnetic interactions.

The field ( $H$ ) dependence of molar magnetization ( $M(H)$ ) of the complexes were studied in the temperature and field-range of 2 to 5 K and 0 to 7 T, respectively. For  $[\text{Gd}_2]$ , saturation of the magnetization is reached at fields larger than 3 T. The  $M(H) = 13.9 \mu_B$  is practically identical to the Brillouin function for two uncoupled  $\text{Gd}^{3+}$  ions (Figure 5a, inset), indicating a negligible interaction between the ions.  $M(H)$  values of 9.2 and  $9.8 \mu_B$ , at an applied magnetic field of 7 T ( $T = 2$  K), were observed for the  $[\text{Tb}_2]$  and  $[\text{Dy}_2]$  (Figure 5b, inset) complexes, respectively.

The downturn in the  $\chi_M T$  profile for  $\text{Gd}_2$  can be quantified by fitting magnetic susceptibility data and the  $M(H)$  employing eq 1:

$$H = -2J\hat{S}_1\hat{S}_2 + g\mu_B H \sum_{i=1}^2 \hat{S}_i \quad (1)$$

where the first term is the isotropic interaction connecting the spins, and the second is the Zeeman term. Simultaneous fitting<sup>69</sup> yields an exchange coupling ( $J$ ) value of  $-13$  mK ( $-0.01 \text{ cm}^{-1}$ ) with  $g = 1.99$  (Figure 4). The magnitude of  $J$  obtained from fitting procedure is in the range ( $J_{\text{dip}} = -0.01 \text{ cm}^{-1}$ ) expected for dipolar interactions associated with two  $\text{Gd}^{3+}$  centers. At this stage, no further analysis of the magnetic data for the systems based on anisotropic lanthanide ions is possible.

To assess the SMM behavior of the complexes, alternating current (AC) magnetic susceptibility measurements were performed in an oscillating field of 5 Oe. No SMM characteristics were found for the Tb complex, as inferred

from the absence of clear peaks in the out-of-phase ( $\chi''$ ) susceptibility measurements (Figure S8). In contrast, a frequency and temperature dependence of the magnetic susceptibility, characteristic of SMM behavior, were observed for  $[\text{Dy}_2]$  at zero applied magnetic field (Figure 6a). Application of an optimal DC magnetic field of 600 Oe (Figure S9 and Table S4) resulted in the shifting of the  $\chi''$  peaks to a low frequency regime, as depicted in Figure 6b.

At zero applied magnetic field, temperature  $\chi_M''(T)$  and frequency dependent  $\chi_M''(\nu)$  out-of-phase magnetic susceptibilities, were observed for  $[\text{Dy}_2]$ . Temperature dependence of relaxation time ( $\tau(T)$ ) was extracted by fitting the  $\chi_M''(\nu)$  data to a modified Debye process between 2 and 7 K. As shown in Figure 6c, a linear trend is observed above 5 K, which is characteristic of the Orbach process, whereas quantum tunnelling of magnetization (QTM) is active below 4 K. The  $\tau(T)$  can be fitted by eq 2:

$$\tau^{-1} = \tau_0^{-1} \exp[-U_{\text{eff}}/T] + CT^n + \tau_{\text{QTM}}^{-1} \quad (2)$$

where the first, second, and third terms represent the Orbach, Raman, and QTM processes, respectively. Fitting the data for the Dy complex at  $H_{\text{DC}} = 0$  affords:  $U_{\text{eff}} = 29.7(1)$  K,  $\tau_0 = 2.92(6) \times 10^{-6}$  s,  $C = 0.0042(6) \text{ s}^{-1} \text{ K}^{-n}$ ,  $n = 6.236$ , and  $\tau_{\text{QTM}} = 3.54(5) \times 10^{-4}$  s. Application of an optimal DC field of 600 Oe reduces the relaxation rate (Figure 5b,c). Fitting of the  $\tau(T)$  plot obtained at  $H_{\text{DC}} = 600$  Oe yields the following parameters:  $U_{\text{eff}} = 39.2(1)$  K,  $\tau_0 = 2.18 \times 10^{-6}$  s,  $C = 0.0026(1) \text{ s}^{-1} \text{ K}^{-n}$ ,  $n = 6.685(2)$ , and  $\tau_{\text{QTM}} = 0.032(2)$  s.

To gain further insight into the magnetization blocking of the Dy complex, *ab initio* calculations were performed with the CASSCF/SO-RASSI/SINGLE\_ANISO approach implemented in the Molcas 8.2 program package.<sup>70–72</sup> For this purpose, the atomic coordinates of the Dy complex obtained from the single-crystal study were used without further

optimization. The energies of the low-lying Kramer's doublets and the main components of the  $g$  tensor of the  $\text{Dy}^{3+}$  are given in Table 2. The main magnetic axis ( $z$ ) on the Dy ions is

**Table 2.** *Ab Initio* Energy Barrier and Principal  $g$ -Tensor for the Kramer Doublets of  $[\text{Dy}_2]^{a}$

ab initio energy (cm <sup>-1</sup> )	ab initio energy (K)	$g_x$	$g_y$	$g_z$	angle (deg)
0	0	0.1070	0.2223	19.4381	-
76.0	109.4	0.33685	1.1329	16.5012	121.6
101.2	145.6	0.9737	3.9503	11.3464	147.1
155.3	223.4	3.0891	6.2096	9.3338	98.7
200.9	289.1	0.3617	2.9396	10.9491	86.8
260.3	374.5	1.0746	2.4783	13.9358	101.4
286.7	412.5	1.1822	3.5791	13.7718	75.8
326.5	469.8	0.7302	0.0355	17.5599	55.7

<sup>a</sup>The wave function for the ground state is 99%  $|\pm 15/2\rangle$ , while the first excited state is 97%  $|\pm 13/2\rangle + 2\% |\pm 11/2\rangle$ .

indicated in Figure 1 by the yellow arrow, which is perpendicular to Cl. The  $g$ -values,  $g_x = 0.1$ ,  $g_y = 0.3$ , and  $g_z = 19.43$ , indicate the axial nature of ground state doublet. The first excited state lies at 76 cm<sup>-1</sup>, the second excited state is at 101 cm<sup>-1</sup>, and subsequent excited states are mixed and lie in the range of 155 to 330 cm<sup>-1</sup> above the ground state doublet. The ground state doublet can be described as  $m_J = \pm 15/2$ , while the first excited state is mainly  $\pm 13/2$  (97%). The average matrix elements of magnetic moment between the electronic states suggest the most efficient magnetic relaxation pathway to occur *via* the first excited state at 76 cm<sup>-1</sup> (110 K). As observed, the  $U_{\text{eff}} = 20.64$  cm<sup>-1</sup> ( $H_{\text{DC}} = 0$  Oe) obtained from dynamic studies is lower than the separation ( $\Delta E = 76$  cm<sup>-1</sup>) of the ground and first excited state, indicating the importance of anharmonic processes in the relaxation of the complexes,<sup>73</sup> while application of an optimal field reduces relaxation leading to  $\Delta E \approx 40$  cm<sup>-1</sup>.

Employing the crystal field parameters obtained from the CASSCF calculation and connecting the two anisotropic  $\text{Dy}^{3+}$  ions via an isotropic exchange interaction, via the Lines model, we were able to simultaneously fit the  $\chi_M''(T)$  and  $M(H)$  data with an exchange Ising Hamiltonian of the form:

$$\hat{H}_{\text{ex}} = J_{\text{Lines}}(\hat{S}_{1,z} + \hat{S}_{2,z}) \quad (3)$$

where  $J_{\text{Lines}}$  is the exchange interaction connecting the spin part of the  $\text{Dy}^{3+}$ ; that is,  $S = 5/2$ . We are able to reproduce the data sets with  $J_{\text{Lines}} = -0.04$  cm<sup>-1</sup> (Figure 5b). Comparison of the dipolar interaction between the  $\text{Dy}^{3+}$  and the  $J_{\text{Lines}}$  suggests that the interaction between the spins is purely of dipolar origin.

## CONCLUSIONS

A new set of stable and charge-neutral binuclear lanthanide complexes of molecular formula  $[\text{Ln}_2\text{Cl}_6(\text{picNO})_4(\mu_2\text{-picNO})_2]\cdot 2\text{H}_2\text{O}$  ( $\text{Ln} = \text{Tb}$  or  $\text{Dy}$ ) was synthesized. Crystal structure analyses of the complexes revealed pentagonal bipyramidal geometry around the lanthanide ions. The 4-picNO ligand photosensitizes the  $\text{Tb}^{3+}$  and  $\text{Dy}^{3+}$  centered emission; total PL quantum yields of 88% ( $[\text{Tb}_2]$ ) and 0.14% ( $[\text{Dy}_2]$ ) were determined in the solid state. The optimal energy gap ( $\Delta E = \sim 3310$  cm<sup>-1</sup>) between the ligand-centered triplet (donor) and  $\text{Tb}^{3+}$ -centered  $^5\text{D}_4$  receiving level facilitated efficient Tb-centered emission. From the SMM front, the Dy-

complex functioned as an SMM in the absence of an applied magnetic field, and the application of a small DC field (600 Oe) slightly increased the spin-reversal barrier by suppressing the QTM. No out-of-phase susceptibility peaks were observed for the  $[\text{Tb}_2]$  complex at zero and applied magnetic fields, indicating the absence of the slow relaxation of the magnetization in the complex. Fitting of the  $M(H)$  plot of the Gd<sub>2</sub>-complex with a Hamiltonian involving isotropic exchange interaction revealed the presence of weak intramolecular dipolar interaction mediated antiferromagnetic coupling between the constituent  $\text{Gd}^{3+}$ -centers. Further, the weakly luminescent nature of the  $[\text{Dy}_2]$  complex coupled with the not so well resolved fine structure of the  $^4\text{F}_{9/2} \rightarrow ^6\text{H}_{15/2}$  luminescence band centered at 485 nm rendered difficult the possibility to establish a magneto-optical correlation based on PL measurements. Overall, the easy-to-prepare nature of the complexes, the high 88% PL quantum yield obtained for the Tb-complex, and the SMM characteristic of the Dy-complex in the absence of an applied magnetic field are the salient aspects of this study.

## EXPERIMENTAL SECTION

**Materials.** 4-Picoline-*N*-oxide,  $\text{TbCl}_3\cdot 6\text{H}_2\text{O}$ ,  $\text{DyCl}_3\cdot 6\text{H}_2\text{O}$ , and the solvents used in this study are received from commercial sources and used as received.

**General Procedure for the Synthesis of the  $[\text{Ln}_2\text{Cl}_6(\text{PicNO})_4(\mu_2\text{-PicNO})_2]\cdot 2\text{H}_2\text{O}$  ( $\text{Ln} = \text{Tb}$  and  $\text{Dy}$ ) Complexes.** To a solution of 0.35 g (3.2 mmol) of 4-picoline-*N*-oxide in 12 mL of  $\text{H}_2\text{O}$ , 1.07 mmol of  $\text{LnCl}_3\cdot 6\text{H}_2\text{O}$  ( $\text{Ln} = \text{Tb}$  or  $\text{Dy}$ ) was added as a solid. The reaction mixture was stirred for 10 min, and water was evaporated from the reaction mixture under reduced pressure. The solids were redissolved in 15 mL of hot EtOH and filtered, and the filtrate was cooled to RT. About 15–20 mL of EtOAc was carefully added to the filtrate until the formation of slight turbidity/precipitate, and the mixture was filtered to obtain a clear solution. The clear solution was left undisturbed for a few days in a closed vial. The procedure yielded X-ray quality crystals of  $[\text{Ln}_2\text{Cl}_6(\text{picNO})_4(\mu_2\text{-picNO})_2]\cdot 2\text{H}_2\text{O}$  ( $\text{Ln} = \text{Tb}$  or  $\text{Dy}$ ) in about 60% yield. The crystalline complexes are stable and can be stored and handled at ambient conditions.

**Elemental Analysis.**  $[\text{Tb}_2\text{Cl}_6(\text{picNO})_4(\mu_2\text{-picNO})_2]\cdot 2\text{H}_2\text{O}$ : Calculated for  $\text{C}_{36}\text{H}_{42}\text{Cl}_6\text{Tb}_2\text{N}_6\text{O}_6\cdot 2\text{H}_2\text{O}$ , C 35.4, H 3.8, N 6.88; Found C 34.93, H 3.73, N 6.76.

$[\text{Dy}_2\text{Cl}_6(\text{picNO})_4(\mu_2\text{-picNO})_2]\cdot 2\text{H}_2\text{O}$ : Calculated for  $\text{C}_{36}\text{H}_{42}\text{Cl}_6\text{Dy}_2\text{N}_6\text{O}_6\cdot 2\text{H}_2\text{O}$ , C 35.20, H 3.77, N 6.84; Found C 35.07, H 3.70, N 6.78.

**Infrared Spectroscopic Studies.** Attenuated total reflectance infrared (ATR-IR) spectroscopic studies of 4-picoline-*N*-oxide ligand, and the complexes were performed using a Thermo Scientific Nicolet iSS0 FT-IR spectrometer.

**X-ray Crystallography.** X-ray diffraction data of  $[\text{Tb}_2\text{Cl}_6(\text{PicNO})_4(\mu_2\text{-PicNO})_2]\cdot 2\text{H}_2\text{O}$  were collected employing a STOE StadiVari 2S diffractometer with a Pilatus300 K detector using a GeniX 3D HF micro focus with  $\text{MoK}\alpha$  radiation ( $\lambda = 0.71073$  Å). The structure was solved using direct methods and was refined by full-matrix least-squares methods on all  $F_2$  using SHELX-2014 implemented in Olex2. The crystals were mounted on a glass tip using crystallographic oil and placed in a cryostream. Data were collected using  $\phi$  and  $\omega$  scans chosen to give a complete asymmetric unit. All non-hydrogen atoms were refined anisotropically. Hydrogen atoms were calculated geometrically riding on their parent atoms.

For the  $[\text{Dy}_2\text{Cl}_6(\text{PicNO})_4(\mu_2\text{-PicNO})_2]\cdot 2\text{H}_2\text{O}$  complex, X-ray diffraction data collection was carried out on a Bruker APEX II DUO Kappa-CCD diffractometer equipped with an Oxford Cryosystem liquid  $\text{N}_2$  device, using  $\text{Mo-K}\alpha$  radiation ( $\lambda = 0.71073$  Å). The crystal-detector distance was 38 mm. The cell parameters were determined (APEX3 software; M86-EXX229 V1 APEX3 User

Manual, Bruker AXS Inc., Madison, USA, 2016) from reflections taken from three sets of 12 frames, each at 10 s exposure. The structure was solved using the program SHELXT-2014.<sup>74</sup> The refinement and all further calculations were carried out using SHELXL-2014.<sup>75</sup> Hydrogen atoms were included in calculated positions and treated as riding atoms using SHELXL default parameters. The non-hydrogen atoms were refined anisotropically, using weighted full-matrix least-squares on  $F^2$ .

**Powder X-ray Diffraction Studies.** The PXRD patterns were obtained with a transmission Guinier-like geometry. A linear focalized monochromatic Cu  $K\alpha 1$  beam ( $\lambda = 1.54056 \text{ \AA}$ ) was obtained using a sealed-tube generator (600 W) equipped with a bent quartz monochromator. The samples were filled in sealed cells of adjustable path. The sample temperature was controlled within  $\pm 0.1 \text{ }^\circ\text{C}$ , and exposure times were varied from 4 to 24 h. The patterns were recorded on image plates scanned by Amersham Typhoon IP with 25  $\mu\text{m}$  resolution (periodicities up to 120  $\text{\AA}$ ).  $I(2\theta)$  profiles were obtained from images, by using a home-developed software.

**Magnetism.** DC magnetic susceptibility measurements were performed using Quantum Design MPMS3 and MPMS-XL SQUID magnetometers on crystalline material in the temperature range of 2–300 K under an applied DC magnetic field ( $H$ ) of 1000 Oe. DC data were corrected for diamagnetic contributions from the eicosane and core diamagnetism employing Pascal's constants. Magnetization as a function of an applied field was investigated in the field and temperature ranges of 0–7 T and 2–10 K, respectively, at a sweep rate of 700 Oe/min. AC data were collected using an oscillating magnetic field of 5 Oe and frequencies between 1 and 1.5 kHz.

**Photophysical Studies.** Steady state emission and excitation spectra were recorded on a FLP920 spectrometer from Edinburgh Instrument working with a continuous 450 W Xe lamp and a red sensitive Hamamatsu R928 photomultiplier in Peltier housing. All spectra were corrected for the instrumental functions. When necessary, high pass filters at 330 nm, 395 nm, 455 nm, or 850 nm were used to eliminate the second order artifacts.

Phosphorescence lifetimes were measured on the same instrument working in the Multi Channels Spectroscopy (MCS) mode and using a Xenon flash lamp as the excitation source. Errors on lifetimes are  $\pm 10\%$ . Luminescence quantum yields were measured with a G8 Integrating Sphere (GMP SA, Switzerland) according to the absolute method detailed in the literature.<sup>76</sup> Estimated errors are  $\pm 15\%$ .

Low temperature measurements were performed with the help of an OptistatDN2 thermocryostat from Oxford Instruments controlled by a MercuryITC temperature controller and with a turbopump form HiCUBE.

**Computational Details.** The atoms were described using standard basis sets from the ANO-RCC library available in Molcas. For the lanthanide ion, a basis set of VTZP quality was employed, while VDZP quality was used for the atoms directly attached to the lanthanide ions, and VDZ quality for all remaining atoms. The molecular orbitals (MOs) were optimized in state-averaged CASSCF calculations. For this, the active space for the Dy complex was defined by the nine 4f electrons in the seven 4f orbitals of  $\text{Dy}^{3+}$ . Three calculations were performed independently for each possible spin-state, where 21 roots were included for  $S = 5/2$ , 224 roots were included for  $S = 3/2$ , and 490 roots were for  $S = 1/2$  (RASSCF routine). The wave functions obtained from these CASSCF calculations were posteriorly mixed by spin-orbit coupling, where all 21  $S = 5/2$  states, 128 of the  $S = 3/2$  states, and 130 of the  $S = 1/2$  states were included (RASSI routine).

## AUTHOR INFORMATION

### Corresponding Authors

**Senthil Kumar Kuppasamy** – *Institute of Quantum Materials and Technologies (IQMT), Karlsruhe Institute of Technology (KIT), 76344 Eggenstein-Leopoldshafen, Germany;*

orcid.org/0000-0002-1501-7759;

Email: [senthil.kuppasamy2@kit.edu](mailto:senthil.kuppasamy2@kit.edu)

**Eufemio Moreno-Pineda** – *Departamento de Química-Física, Facultad de Ciencias Naturales, Exactas y Tecnología, Universidad de Panamá, 0824 Panamá City, Panamá;*

orcid.org/0000-0002-9643-0341;

Email: [eufemio.moreno@up.ac.pa](mailto:eufemio.moreno@up.ac.pa)

**Aline M. Nonat** – *Equipe de Synthèse pour l'Analyse, IPHC, UMR 7178, CNRS-Université de Strasbourg, ECPM, 67087 Strasbourg Cedex, France;*

orcid.org/0000-0003-0478-

5039; Email: [aline.nonat@unistra.fr](mailto:aline.nonat@unistra.fr)

**Mario Ruben** – *Institute of Quantum Materials and Technologies (IQMT), Karlsruhe Institute of Technology (KIT), 76344 Eggenstein-Leopoldshafen, Germany; Institute of Nanotechnology (INT), Karlsruhe Institute of Technology (KIT), D-76344 Eggenstein-Leopoldshafen, Germany; Centre Européen de Sciences Quantiques (CESQ), Institut de Science et d'Ingénierie, Supramoléculaires (ISIS), 67083 Strasbourg Cedex, France; Email: [mario.ruben@kit.edu](mailto:mario.ruben@kit.edu)*

### Authors

**Benoît Heinrich** – *Institut de Physique et Chimie des Matériaux de Strasbourg (IPCMS), CNRS-Université de Strasbourg, 67034 Strasbourg Cedex 2, France;*

orcid.org/0000-0001-6795-2733

**Lydia Karmazin** – *Service de Radiocristallographie, Fédération de Chimie Le Bel FR2010, CNRS-Université de Strasbourg, 67008 Strasbourg Cedex, France*

**Loïc J. Charbonnière** – *Equipe de Synthèse pour l'Analyse, IPHC, UMR 7178, CNRS-Université de Strasbourg, ECPM, 67087 Strasbourg Cedex, France; orcid.org/0000-0003-0328-9842*

### Notes

The authors declare no competing financial interest.

## ACKNOWLEDGMENTS

We acknowledge the DFG-TR 88 “3Met” (project A8) and the Karlsruhe Nano Micro Facility (KNMF, [www.kit.edu/knmf](http://www.kit.edu/knmf)) for provision of access to instruments at their laboratories. E.M.P. acknowledges the Panamanian National System of Investigators (SNI, SENACYT) and the Project PFID-FID-2021-60 for support. AN and LC thank CNRS for support.

## REFERENCES

- (1) Ishikawa, N. Single Molecule Magnet with Single Lanthanide Ion. *Polyhedron* **2007**, *26* (9–11), 2147–2153.



- (2) Ishikawa, N.; Sugita, M.; Ishikawa, T.; Koshihara, S.; Kaizu, Y. Lanthanide Double-Decker Complexes Functioning as Magnets at the Single-Molecule Level. *J. Am. Chem. Soc.* **2003**, *125* (29), 8694–8695.
- (3) Woodruff, D. N.; Winpenny, R. E. P.; Layfield, R. A. Lanthanide Single-Molecule Magnets. *Chem. Rev.* **2013**, *113* (7), 5110–5148.
- (4) Armelao, L.; Quici, S.; Barigelletti, F.; Accorsi, G.; Bottaro, G.; Cavazzini, M.; Tondello, E. Design of Luminescent Lanthanide Complexes: From Molecules to Highly Efficient Photo-Emitting Materials. *Coord. Chem. Rev.* **2010**, *254* (5–6), 487–505.
- (5) Bünzli, J.-C. G.; Piguet, C. Taking Advantage of Luminescent Lanthanide Ions. *Chem. Soc. Rev.* **2005**, *34* (12), 1048.
- (6) Guo, F.-S.; Day, B. M.; Chen, Y.-C.; Tong, M.-L.; Mansikkamäki, A.; Layfield, R. A. Magnetic Hysteresis up to 80 K in a Dysprosium Metallocene Single-Molecule Magnet. *Science* **2018**, *362* (6421), 1400–1403.
- (7) Gould, C. A.; McClain, K. R.; Reta, D.; Kragoskow, J. G. C.; Marchiori, D. A.; Lachman, E.; Choi, E.-S.; Analytis, J. G.; Britt, R. D.; Chilton, N. F.; Harvey, B. G.; Long, J. R. Ultrahard Magnetism from Mixed-Valence Dilanthanide Complexes with Metal-Metal Bonding. *Science* **2022**, *375* (6577), 198–202.
- (8) Goodwin, C. A. P.; Ortu, F.; Reta, D.; Chilton, N. F.; Mills, D. P. Molecular Magnetic Hysteresis at 60 K in Dysprosocenium. *Nature* **2017**, *548* (7668), 439–442.
- (9) Moreno-Pineda, E.; Godfrin, C.; Balestro, F.; Wernsdorfer, W.; Ruben, M. Molecular Spin Qubits for Quantum Algorithms. *Chem. Soc. Rev.* **2018**, *47* (2), 501–513.
- (10) Moreno-Pineda, E.; Klyatskaya, S.; Du, P.; Damjanović, M.; Taran, G.; Wernsdorfer, W.; Ruben, M. Observation of Cooperative Electronic Quantum Tunneling: Increasing Accessible Nuclear States in a Molecular Qudit. *Inorg. Chem.* **2018**, *57* (16), 9873–9879.
- (11) Gaita-Ariño, A.; Luis, F.; Hill, S.; Coronado, E. Molecular Spins for Quantum Computation. *Nat. Chem.* **2019**, *11* (4), 301–309.
- (12) Moreno-Pineda, E.; Wernsdorfer, W. Measuring Molecular Magnets for Quantum Technologies. *Nat. Rev. Phys.* **2021**, *3* (9), 645–659.
- (13) Bogani, L.; Wernsdorfer, W. Molecular Spintronics Using Single-Molecule Magnets. *Nat. Mater.* **2008**, *7* (3), 179–186.
- (14) Urdampilleta, M.; Klyatskaya, S.; Cleuziou, J.-P.; Ruben, M.; Wernsdorfer, W. Supramolecular Spin Valves. *Nat. Mater.* **2011**, *10* (7), 502–506.
- (15) Wagner, S.; Kisslinger, F.; Ballmann, S.; Schramm, F.; Chandrasekar, R.; Bodenstein, T.; Fuhr, O.; Secker, D.; Fink, K.; Ruben, M.; Weber, H. B. Switching of a Coupled Spin Pair in a Single-Molecule Junction. *Nat. Nanotechnol.* **2013**, *8* (8), 575–579.
- (16) Thiele, S.; Balestro, F.; Ballou, R.; Klyatskaya, S.; Ruben, M.; Wernsdorfer, W. Electrically Driven Nuclear Spin Resonance in Single-Molecule Magnets. *Science* **2014**, *344* (6188), 1135–1138.
- (17) Vincent, R.; Klyatskaya, S.; Ruben, M.; Wernsdorfer, W.; Balestro, F. Electronic Read-out of a Single Nuclear Spin Using a Molecular Spin Transistor. *Nature* **2012**, *488* (7411), 357–360.
- (18) Feng, M.; Tong, M.-L. Single Ion Magnets from 3d to 5f: Developments and Strategies. *Chem. - Eur. J.* **2018**, *24* (30), 7574–7594.
- (19) Zhang, P.; Guo, Y.-N.; Tang, J. Recent Advances in Dysprosium-Based Single Molecule Magnets: Structural Overview and Synthetic Strategies. *Coord. Chem. Rev.* **2013**, *257* (11–12), 1728–1763.
- (20) Gupta, S. K.; Murugavel, R. Enriching Lanthanide Single-Ion Magnetism through Symmetry and Axiality. *Chem. Commun.* **2018**, *54* (30), 3685–3696.
- (21) Ungur, L.; Chibotaru, L. F. Strategies toward High-Temperature Lanthanide-Based Single-Molecule Magnets. *Inorg. Chem.* **2016**, *55* (20), 10043–10056.
- (22) Sessoli, R.; Powell, A. K. Strategies towards Single Molecule Magnets Based on Lanthanide Ions. *Coord. Chem. Rev.* **2009**, *253* (19–20), 2328–2341.
- (23) Scherthan, L.; Schmidt, S. F. M.; Auerbach, H.; Hochdörffer, T.; Wolny, J. A.; Bi, W.; Zhao, J.; Hu, M. Y.; Toellner, T.; Alp, E. E.; Brown, D. E.; Anson, C. E.; Powell, A. K.; Schünemann, V. <sup>161</sup>Dy Time-Domain Synchrotron Mössbauer Spectroscopy for Investigating Single-Molecule Magnets Incorporating Dy Ions. *Angew. Chem., Int. Ed.* **2019**, *58* (11), 3444–3449.
- (24) Bünzli, J.-C. G. On the Design of Highly Luminescent Lanthanide Complexes. *Coord. Chem. Rev.* **2015**, *293–294*, 19–47.
- (25) Sy, M.; Nonat, A.; Hildebrandt, N.; Charbonnière, L. J. Lanthanide-Based Luminescence Biolabelling. *Chem. Commun.* **2016**, *52* (29), 5080–5095.
- (26) Tangoulis, V.; Nastopoulos, V.; Panagiotou, N.; Tasiopoulos, A.; Itskos, G.; Athanasiou, M.; Moreno-Pineda, E.; Wernsdorfer, W.; Schulze, M.; Malina, O. High-Performance Luminescence Thermometer with Field-Induced Slow Magnetic Relaxation Based on a Heterometallic Cyanido-Bridged 3d–4f Complex. *Inorg. Chem.* **2022**, *61* (5), 2546–2557.
- (27) Karachousos-Spiliotakopoulos, K.; Tangoulis, V.; Panagiotou, N.; Tasiopoulos, A.; Moreno-Pineda, E.; Wernsdorfer, W.; Schulze, M.; Botas, A. M. P.; Carlos, L. D. Luminescence Thermometry and Field Induced Slow Magnetic Relaxation Based on a near Infrared Emissive Heterometallic Complex. *Dalton Trans.* **2022**, *51* (21), 8208–8216.
- (28) Dolai, M.; Moreno-Pineda, E.; Wernsdorfer, W.; Ali, M.; Ghosh, A. Exchange-Bias Quantum Tunneling of the Magnetization in a Dysprosium Dimer. *J. Phys. Chem. A* **2021**, *125* (37), 8230–8237.
- (29) Randall McClain, K.; Gould, C. A.; Chakarawet, K.; Teat, S. J.; Groshens, T. J.; Long, J. R.; Harvey, B. G. High-Temperature Magnetic Blocking and Magneto-Structural Correlations in a Series of Dysprosium(III) Metallocenium Single-Molecule Magnets. *Chem. Sci.* **2018**, *9* (45), 8492–8503.
- (30) Day, B. M.; Guo, F.-S.; Layfield, R. A. Cyclopentadienyl Ligands in Lanthanide Single-Molecule Magnets: One Ring To Rule Them All? *Acc. Chem. Res.* **2018**, *51* (8), 1880–1889.
- (31) Ding, Y.; Han, T.; Zhai, Y.; Reta, D.; Chilton, N. F.; Winpenny, R. E. P.; Zheng, Y. A Study of Magnetic Relaxation in Dysprosium-(III) Single-Molecule Magnets. *Chem. - Eur. J.* **2020**, *26* (26), 5893–5902.
- (32) Evans, P.; Reta, D.; Whitehead, G. F. S.; Chilton, N. F.; Mills, D. P. Bis-Monophospholyl Dysprosium Cation Showing Magnetic Hysteresis at 48 K. *J. Am. Chem. Soc.* **2019**, *141* (50), 19935–19940.
- (33) Han, T.; Giansiracusa, M. J.; Li, Z.; Ding, Y.; Chilton, N. F.; Winpenny, R. E. P.; Zheng, Y. Exchange-Biasing in a Dinuclear Dysprosium(III) Single-Molecule Magnet with a Large Energy Barrier for Magnetisation Reversal. *Chem. - Eur. J.* **2020**, *26* (30), 6773–6777.
- (34) Wu, H.; Li, M.; Xia, Z.; Montigaud, V.; Cador, O.; Le Guennic, B.; Ke, H.; Wang, W.; Xie, G.; Chen, S.; Gao, S. High Temperature Quantum Tunneling of Magnetization and Thousand Kelvin Anisotropy Barrier in a Dy<sub>2</sub> Single-Molecule Magnet. *Chem. Commun.* **2021**, *57* (3), 371–374.
- (35) Zhu, Z.; Zhao, C.; Feng, T.; Liu, X.; Ying, X.; Li, X.-L.; Zhang, Y.-Q.; Tang, J. Air-Stable Chiral Single-Molecule Magnets with Record Anisotropy Barrier Exceeding 1800 K. *J. Am. Chem. Soc.* **2021**, *143* (27), 10077–10082.
- (36) Zhu, Z.; Tang, J. Metal–Metal Bond in Lanthanide Single-Molecule Magnets. *Chem. Soc. Rev.* **2022**, *51* (23), 9469–9481.
- (37) Ashebr, T. G.; Li, H.; Ying, X.; Li, X.-L.; Zhao, C.; Liu, S.; Tang, J. Emerging Trends on Designing High-Performance Dysprosium(III) Single-Molecule Magnets. *ACS Mater. Lett.* **2022**, *4* (2), 307–319.
- (38) Ding, Y.-S.; Deng, Y.-F.; Zheng, Y.-Z. The Rise of Single-Ion Magnets as Spin Qubits. *Magnetochemistry* **2016**, *2* (4), 40.
- (39) Pedersen, K. S.; Ariciu, A.-M.; McAdams, S.; Weihe, H.; Bendix, J.; Tuna, F.; Piligkos, S. Toward Molecular 4f Single-Ion Magnet Qubits. *J. Am. Chem. Soc.* **2016**, *138* (18), 5801–5804.
- (40) Escalera-Moreno, L.; Baldoví, J. J.; Gaita-Ariño, A.; Coronado, E. Spin States, Vibrations and Spin Relaxation in Molecular Nanomagnets and Spin Qubits: A Critical Perspective. *Chem. Sci.* **2018**, *9* (13), 3265–3275.

- (41) Wernsdorfer, W.; Ruben, M. Synthetic Hilbert Space Engineering of Molecular Qu *d* Its: Isotopologue Chemistry. *Adv. Mater.* **2019**, *31* (26), No. 1806687.
- (42) Jenkins, M. D.; Duan, Y.; Diosdado, B.; García-Ripoll, J. J.; Gaita-Ariño, A.; Giménez-Saiz, C.; Alonso, P. J.; Coronado, E.; Luis, F. Coherent Manipulation of Three-Qubit States in a Molecular Single-Ion Magnet. *Phys. Rev. B* **2017**, *95* (6), No. 064423.
- (43) Ferrando-Soria, J.; Moreno Pineda, E.; Chiesa, A.; Fernandez, A.; Magee, S. A.; Carretta, S.; Santini, P.; Vitorica-Yrezabal, I. J.; Tuna, F.; Timco, G. A.; McInnes, E. J. L.; Winpenny, R. E. P. A Modular Design of Molecular Qubits to Implement Universal Quantum Gates. *Nat. Commun.* **2016**, *7* (1), No. 11377.
- (44) Biard, H.; Moreno-Pineda, E.; Ruben, M.; Bonet, E.; Wernsdorfer, W.; Balestro, F. Increasing the Hilbert Space Dimension Using a Single Coupled Molecular Spin. *Nat. Commun.* **2021**, *12* (1), 4443.
- (45) Moreno-Pineda, E.; Damjanović, M.; Fuhr, O.; Wernsdorfer, W.; Ruben, M. Nuclear Spin Isomers: Engineering a Et<sub>4</sub>N[DyPc<sub>2</sub>] Spin Qudit. *Angew. Chem., Int. Ed.* **2017**, *56* (33), 9915–9919.
- (46) Moreno-Pineda, E.; Taran, G.; Wernsdorfer, W.; Ruben, M. Quantum Tunnelling of the Magnetisation in Single-Molecule Magnet Isotopologue Dimers. *Chem. Sci.* **2019**, *10* (19), 5138–5145.
- (47) Godfrin, C.; Ferhat, A.; Ballou, R.; Klyatskaya, S.; Ruben, M.; Wernsdorfer, W.; Balestro, F. Operating Quantum States in Single Magnetic Molecules: Implementation of Grover's Quantum Algorithm. *Phys. Rev. Lett.* **2017**, *119* (18), No. 187702.
- (48) Binnemans, K. Interpretation of Europium(III) Spectra. *Coord. Chem. Rev.* **2015**, *295*, 1–45.
- (49) Utochnikova, V. V.; Kalyakina, A. S.; Bushmarinov, I. S.; Vashchenko, A. A.; Marciniak, L.; Kaczmarek, A. M.; Van Deun, R.; Bräse, S.; Kuzmina, N. P. Lanthanide 9-Anthracenate: Solution Processable Emitters for Efficient Purely NIR Emitting Host-Free OLEDs. *J. Mater. Chem. C* **2016**, *4* (41), 9848–9855.
- (50) He, H. Near-Infrared Emitting Lanthanide Complexes of Porphyrin and BODIPY Dyes. *Coord. Chem. Rev.* **2014**, *273*–274, 87–99.
- (51) Hu, J.-Y.; Ning, Y.; Meng, Y.-S.; Zhang, J.; Wu, Z.-Y.; Gao, S.; Zhang, J.-L. Highly Near-IR Emissive Ytterbium(III) Complexes with Unprecedented Quantum Yields. *Chem. Sci.* **2017**, *8* (4), 2702–2709.
- (52) George, T. M.; Varughese, S.; Reddy, M. L. P. Near-Infrared Luminescence of Nd<sup>3+</sup> and Yb<sup>3+</sup> Complexes Using a Polyfluorinated Pyrene-Based  $\beta$ -Diketonate Ligand. *RSC Adv.* **2016**, *6* (73), 69509–69520.
- (53) Feng, J.; Zhang, H. Hybrid Materials Based on Lanthanide Organic Complexes: A Review. *Chem. Soc. Rev.* **2013**, *42* (1), 387–410.
- (54) Fataftah, M. S.; Bayliss, S. L.; Laorenza, D. W.; Wang, X.; Phelan, B. T.; Wilson, C. B.; Mintun, P. J.; Kovos, B. D.; Wasielewski, M. R.; Han, S.; Sherwin, M. S.; Awschalom, D. D.; Freedman, D. E. Trigonal Bipyramidal V<sup>3+</sup> Complex as an Optically Addressable Molecular Qubit Candidate. *J. Am. Chem. Soc.* **2020**, *142* (48), 20400–20408.
- (55) Atzori, M.; Santanni, F.; Breslavetz, I.; Paillet, K.; Caneschi, A.; Rikken, G. L. J. A.; Sessoli, R.; Train, C. Magnetic Anisotropy Drives Magnetochemical Dichroism in a Chiral Molecular Helix Probed with Visible Light. *J. Am. Chem. Soc.* **2020**, *142* (32), 13908–13916.
- (56) Bayliss, S. L.; Laorenza, D. W.; Mintun, P. J.; Kovos, B. D.; Freedman, D. E.; Awschalom, D. D. Optically Addressable Molecular Spins for Quantum Information Processing. *Science* **2020**, *370* (6522), 1309–1312.
- (57) Wojnar, M. K.; Laorenza, D. W.; Schaller, R. D.; Freedman, D. E. Nickel(II) Metal Complexes as Optically Addressable Qubit Candidates. *J. Am. Chem. Soc.* **2020**, *142* (35), 14826–14830.
- (58) Kumar, K. S.; Serrano, D.; Nonat, A. M.; Heinrich, B.; Karmazin, L.; Charbonnière, L. J.; Goldner, P.; Ruben, M. Optical Spin-State Polarization in a Binuclear Europium Complex towards Molecule-Based Coherent Light-Spin Interfaces. *Nat. Commun.* **2021**, *12* (1), 2152.
- (59) Serrano, D.; Kuppasamy, S. K.; Heinrich, B.; Fuhr, O.; Hunger, D.; Ruben, M.; Goldner, P. Ultra-Narrow Optical Linewidths in Rare-Earth Molecular Crystals. *Nature* **2022**, *603* (7900), 241–246.
- (60) Nonat, A.; Bahamyrou, S.; Lecointre, A.; Przybilla, F.; Mély, Y.; Platas-Iglesias, C.; Camerel, F.; Jeannin, O.; Charbonnière, L. J. Molecular Upconversion in Water in Heteropolynuclear Supramolecular Tb/Yb Assemblies. *J. Am. Chem. Soc.* **2019**, *141* (4), 1568–1576.
- (61) Nonat, A.; Chan, C. F.; Liu, T.; Platas-Iglesias, C.; Liu, Z.; Wong, W.-T.; Wong, W.-K.; Wong, K.-L.; Charbonnière, L. J. Room Temperature Molecular up Conversion in Solution. *Nat. Commun.* **2016**, *7* (1), No. 11978.
- (62) Long, J.; Guari, Y.; Ferreira, R. A. S.; Carlos, L. D.; Larionova, J. Recent Advances in Luminescent Lanthanide Based Single-Molecule Magnets. *Coord. Chem. Rev.* **2018**, *363*, 57–70.
- (63) Marin, R.; Brunet, G.; Murugesu, M. Shining New Light on Multifunctional Lanthanide Single-Molecule Magnets. *Angew. Chem., Int. Ed.* **2021**, *60* (4), 1728–1746.
- (64) Jia, J.-H.; Li, Q.-W.; Chen, Y.-C.; Liu, J.-L.; Tong, M.-L. Luminescent Single-Molecule Magnets Based on Lanthanides: Design Strategies, Recent Advances and Magneto-Luminescent Studies. *Coord. Chem. Rev.* **2019**, *378*, 365–381.
- (65) Gállico, D. A.; Marin, R.; Brunet, G.; Errulat, D.; Hemmer, E.; Sigoli, F. A.; Moilanen, J. O.; Murugesu, M. Triplet-State Position and Crystal-Field Tuning in Opto-Magnetic Lanthanide Complexes: Two Sides of the Same Coin. *Chem. – Eur. J.* **2019**, *25* (64), 14625–14637.
- (66) Mamontova, E.; Long, J.; Ferreira, R.; Botas, A.; Luneau, D.; Guari, Y.; Carlos, L.; Larionova, J. Magneto-Luminescence Correlation in the Textbook Dysprosium(III) Nitrate Single-Ion Magnet. *Magnetochemistry* **2016**, *2* (4), 41.
- (67) Norel, L.; Darago, L. E.; Le Guennic, B.; Chakarawet, K.; Gonzalez, M. I.; Olshansky, J. H.; Rigaut, S.; Long, J. R. A Terminal Fluoride Ligand Generates Axial Magnetic Anisotropy in Dysprosium Complexes. *Angew. Chem., Int. Ed.* **2018**, *57* (7), 1933–1938.
- (68) Vijayakumar, M.; Marimuthu, K.; Sudarsan, V. Concentration Dependent Spectroscopic Behavior of Sm<sup>3+</sup> Doped Leadfluoro-Borophosphate Glasses for Laser and LED Applications. *J. Alloys Compd.* **2015**, *647*, 209–220.
- (69) Chilton, N. F.; Anderson, R. P.; Turner, L. D.; Soncini, A.; Murray, K. S. PHI: A Powerful New Program for the Analysis of Anisotropic Monomeric and Exchange-Coupled Polynuclear *d*- and *f*-Block Complexes. *J. Comput. Chem.* **2013**, *34* (13), 1164–1175.
- (70) Aquilante, F.; Autschbach, J.; Carlson, R. K.; Chibotaru, L. F.; Delcey, M. G.; De Vico, L.; Fdez. Galvan, I.; Ferre, N.; Frutos, L. M.; Gagliardi, L.; Garavelli, M.; Giussani, A.; Hoyer, C. E.; Li Manni, G.; Lischka, H.; Ma, D.; Malmqvist, P. A.; Muller, T.; Nenov, A.; Olivucci, M.; Pedersen, T. B.; Peng, D.; Plasser, F.; Pritchard, B.; Reiher, M.; Rivalta, I.; Schapiro, I.; Segarra-Martí, J.; Stenrup, M.; Truhlar, D. G.; Ungur, L.; Valentini, A.; Vancoillie, S.; Veryazov, V.; Vysotskiy, V. P.; Weingart, O.; Zapata, F.; Lindh, R. MOLCAS 8: New Capabilities for Multiconfigurational Quantum Chemical Calculations across the Periodic Table. *J. Comput. Chem.* **2016**, *37* (5), 506–541.
- (71) Siegbahn, P. E. M.; Almlöf, J.; Heiberg, A.; Roos, B. O. The Complete Active Space SCF (CASSCF) Method in a Newton–Raphson Formulation with Application to the HNO Molecule. *J. Chem. Phys.* **1981**, *74* (4), 2384–2396.
- (72) Olsen, J.; Roos, B. O.; Jørgensen, P.; Jensen, H. J. A. Determinant Based Configuration Interaction Algorithms for Complete and Restricted Configuration Interaction Spaces. *J. Chem. Phys.* **1988**, *89* (4), 2185–2192.
- (73) Lunghi, A.; Totti, F.; Sanvito, S.; Sessoli, R. Intra-Molecular Origin of the Spin-Phonon Coupling in Slow-Relaxing Molecular Magnets. *Chem. Sci.* **2017**, *8* (9), 6051–6059.
- (74) Sheldrick, G. M. SHELXT – Integrated Space-Group and Crystal-Structure Determination. *Acta Crystallogr. Sect. Found. Adv.* **2015**, *71* (1), 3–8.

(75) Sheldrick, G. M. Crystal Structure Refinement with *SHELXL*. *Acta Crystallogr. Sect. C Struct. Chem.* **2015**, *71* (1), 3–8.

(76) Wang, Z.; Liu, N.; Li, H.; Chen, P.; Yan, P. The Role of Blue-Emissive 1,8-Naphthalimidopyridine *N*-Oxide in Sensitizing Eu<sup>III</sup> Photoluminescence in Dimeric Hexafluoroacetylacetonate Complexes. *Eur. J. Inorg. Chem.* **2017**, *2017* (15), 2211–2219.